Journal of
Marine Science and Engineering

MDPI

Article

Optimizing Infragravity Wave Attenuation to Improve Coral Reef Restoration Design for Coastal Defense

Benjamin K. Norris [1,*], Curt D. Storlazzi [2], Andrew W. M. Pomeroy [3] and Borja G. Reguero [1]

[1] Institute of Marine Sciences, University of California, Santa Cruz, 115 McAllister Way, Santa Cruz, CA 95060, USA; breguero@ucsc.edu
[2] US Geological Survey, Pacific Coastal and Marine Science Center, 2885 Mission Street, Santa Cruz, CA 95060, USA; cstorlazzi@usgs.gov
[3] School of BioSciences, Biosciences 4, The University of Melbourne, Royal Parade, Parkville, VIC 3052, Australia; a.pomeroy@unimelb.edu.au
* Correspondence: bknorris@ucsc.edu

Abstract: Coral reefs are effective natural flood barriers that protect adjacent coastal communities. As the need to adapt to rising sea levels, storms, and environmental changes increases, reef restoration may be one of the best tools available to mitigate coastal flooding along tropical coastlines, now and in the future. Reefs act as a barrier to incoming short-wave energy but can amplify low-frequency infragravity waves that, in turn, drive coastal flooding along low-lying tropical coastlines. Here, we investigate whether the spacing of reef restoration elements can be optimized to maximize infragravity wave energy dissipation while minimizing the number of elements—a key factor in the cost of a restoration project. With this goal, we model the hydrodynamics of infragravity wave dissipation over a coral restoration or artificial reef, represented by a canopy of idealized hemispherical roughness elements, using a three-dimensional Navier–Stokes equations solver (OpenFOAM). The results demonstrate that denser canopies of restoration elements produce greater wave dissipation under larger waves with longer periods. Wave dissipation is also frequency-dependent: dense canopies remove wave energy at the predominant wave frequency, whereas sparse canopies remove energy at higher frequencies, and hence are less efficient. We also identify an inflection point in the canopy density–energy dissipation curve that balances optimal energy losses with a minimum number of canopy elements. Through this work, we show that there are an ideal number of restoration elements per across-shore meter of coral reef flat that can be installed to dissipate infragravity wave energy for given incident heights and periods. These results have implications for designing coral reef restoration projects on reef flats that are effective both from a coastal defense and costing standpoint.

Keywords: coral reef; coral restoration; wave dissipation; roughness; infragravity waves; numerical modelling; OpenFOAM; canopy flow

Citation: Norris, B.K.; Storlazzi, C.D.; Pomeroy, A.W.M.; Reguero, B.G. Optimizing Infragravity Wave Attenuation to Improve Coral Reef Restoration Design for Coastal Defense. *J. Mar. Sci. Eng.* **2024**, *12*, 768. https://doi.org/10.3390/jmse12050768

Academic Editor: Achilleas Samaras

Received: 10 February 2024
Revised: 26 April 2024
Accepted: 30 April 2024
Published: 1 May 2024

1. Introduction

Coastal hazards present a significant risk to their adjacent communities. Along tropical coastlines, coral reefs protect against flooding and erosion by efficiently dissipating incoming wave energy before it reaches shore [1–9]. Globally, thousands of reef-lined tropical coastlines are threatened by pressures such as climate change, sea-level rise, and coral degradation [10]. Most of these coastlines have critical infrastructure, housing, and agriculture within a few meters of mean sea level [11] and are vulnerable to increased flood risk posed by coral degradation offshore [12–15]. As reefs become increasingly impacted, there is growing concern over whether degraded coral reefs can maintain similar coastal protection benefits under present and future sea level scenarios [8,9,16].

Recent work suggests that maintaining reef structural complexity through restoration may be the best solution to mitigate present and future coastal hazards [17–20]. Structural reef reconstruction often involves the placement of individual rock piles or semi-porous

concrete structures to provide the hard substrate onto which coral can be grown [21]. These individual elements could be arranged into submerged breakwaters to provide additional coastal defense benefits [18]. Although pilot reef restoration projects for coastal defense are still relatively scarce [22,23], limited evidence suggests this strategy is effective in reducing hazards [24]. Further, numerical modeling has identified where along the coastline, and where across the reef system, restoration projects could be most valuable. Along coastal Florida and Puerto Rico, Storlazzi et al. [20] determined that the greatest hazard risk reduction could be achieved through shallower restorations that were closer to shore. Roelvink et al. [19] analyzed over 30,000 global coral reef profiles to quantify how the across-shore placement of coral restorations modifies wave-driven runup. For the most common reef typologies, fringing and atoll reefs, the greatest flood-risk reduction could be achieved with coral restorations on the upper fore reef and middle reef flat, due to enhanced wave breaking and frictional dissipation, respectively. Indeed, many studies focusing on resolving modeled wave dynamics at large scales (i.e., across coral reefs) need to parameterize roughness (e.g., [19,25,26]). Similar studies that resolve the effects of waves on small-scale (i.e., coral colony) features are much less common as the computational effort to include such features scales with the resolved resolution of roughness elements.

The coastal defense benefit of coral reefs arises from two sources of wave height reduction: wave breaking and bottom friction. Most coral reefs have an offshore reef crest that is only a few meters deep, where the rapid change in bathymetry causes most (90–99%) incident sea-swell waves ("SS" > 0.04 Hz) to break, depending on the tidal stage [5,27]. However, not all SS wave energy is dissipated, and some are additionally transformed into infragravity ("IG" 0.004–0.04 Hz) and very-low-frequency ("VLF", 0.001–0.004 Hz) waves through non-linear wave–wave interactions and breakpoint forcing on the fore-reef slope [28–30]. This process creates a mixture of short- and long-period waves that propagate shoreward across the reef flat [26,31], where gradually the remaining SS waves, and to a lesser extent IG waves, are attenuated by frictional dissipation [32]. Hence, unbroken IG waves tend to dominate the wave energy spectrum on the inner reef flat [26,29], and as a result, are often the primary contributor to wave runup and coastal flooding [3,9,33]. Therefore, one strategy to diminish coastal flooding in reef environments is to enhance the bottom roughness of the reef flat to dissipate IG wave energy before it reaches shore.

Although the coastal protection benefits of coral reefs have been the subject of several recent studies [8,9,19,20,34] one limitation has been how the bottom roughness created by reef-building organisms is described and quantified. For field studies, the geometry of large bottom roughness is hard to resolve, and hydrodynamic observations are typically sparse enough to necessitate the quantification of reef-aided coastal defense through wave energy flux gradients [29,31,35–37]. Similarly, laboratory and numerical modeling studies focused on reef-scale hydrodynamics may parameterize roughness with bulk drag coefficients [19,26,38] or neglect bottom roughness altogether [8,39,40]. As a result, these larger-scale studies often cannot resolve the dynamics of wave-driven turbulent flows within reefs, a process which drives many important physical and biological functions that are critical for maintaining healthy corals (Davis et al. [41] and references therein) and likely reef restorations. Recent advances in computational fluid dynamics (CFD) models have enabled the simulation of these complex flow patterns within reefs (e.g., [42–45]), though the focus of these studies was not for restoration.

Here, we focus on characterizing the small-scale (i.e., coral colony) hydrodynamics to optimize coral restoration designs for coastal protection. Specifically, we investigate whether there is an optimal balance between maximizing wave energy dissipation (a benefit of the restoration) with a minimal number of restoration elements (individual coral plantations). Using a three-dimensional Navier–Stokes equations solver to simulate cnoidal waves with IG periods over coral reef flats with idealized bottom roughness, we study different coral reef restoration strategies by characterizing how wave dissipation depends on wave conditions and the spacing of reef roughness elements (e.g., coral heads or artificial reef elements). Although restoration project cost is not the primary focus of this study, we

additionally use the model results to determine a restoration design that maximizes wave energy dissipation while minimizing the number of restoration elements, an optimization that represents the most cost-effective design for a given set of wave conditions.

2. Materials and Methods

2.1. Relevant Hydrodynamic Parameters

Across relatively horizontal reef flats, the process of wave attenuation by bottom friction is predominantly controlled by the physical size and density of coral colonies. At the scale of individual corals, wave velocity attenuation varies inversely with the ratio of the wave orbital excursion, a length scale describing the horizontal displacement of water particles beneath successive waves, to the length scale of bed roughness, A_b/k_w [46–49]. Collectively, assemblages of corals over which wave and current energy is dissipated are referred to as "canopies". The term k_w is a canopy property and is commonly defined as either the circular diameter (d) of individual canopy elements (e.g., [45,50]) or as the center-to-center distance between adjacent canopy elements, ΔS. For circular objects, ΔS is related to the number of canopy elements per across-shore meter (n) by $nd = d/\Delta S^2$, and so $\Delta S = n^{-1/2}$ (e.g., [51]), and can be normalized by d to yield a non-dimensional roughness spacing $D = \Delta S/d$.

Across a rough bottom, drag forces at the bed strip energy from wave flows, converting velocity into turbulence. To describe this process, Lowe et al. [46] defined a canopy attenuation parameter α_w as the ratio of in-canopy to free stream wave velocities. Lowe et al. [46] demonstrated that A_b is the single relevant wave parameter affecting flow in the canopy and identified three distinct flow regimes: (1) when canopy density is sufficiently sparse (i.e., when $A_b/k_w \leq 1$), in-canopy velocity reduction is small (α_w is $O(1)$), flows are inertia-dominated and are not greatly affected by canopy elements; (2) a quasi-unidirectional limit when $A_b/k_w > 100$, in-canopy flows are severely reduced by drag (α_w is $O(0.1)$); and (3) a final regime where canopy drag, inertial, and shear forces all contribute to the momentum balance inside the canopy, leading to intermediate velocity attenuation. Wave energy dissipation, often parameterized with a friction factor f_e, scales inversely with α_w and hence decreases with proportional increases in A_b relative to the physical roughness k_w [52]. Here, we calculate A_b and α_w from the modeled free surface and velocity time series, respectively (see Section 2.4) and estimate k_w as ΔS for each model.

2.2. Experimental Design

Experiments were performed with a series of numerical simulations using the open-source computational fluid dynamics modeling framework OpenFOAM, version-1912 [53]. Model scenarios were based on a range of values from observational and modeling studies of IG waves on reef flats reported in the literature (Table 1). Model cases were defined by combinations of incident IG wave heights H_s, incident IG wave periods T_w, the non-dimensional ratio of wave height to water depth (γ), and the ratio of wave height to wavelength (wave steepness; H_s/λ). In general, waves break on coral reef flats when γ = 0.4–0.6 [17] or when H_s/λ = 0.142 [54], but the non-breaking IG waves considered here were well below both of these limits.

Table 1. Literature values from former field and numerical modeling studies for expected range of infragravity wave conditions on reef flats. Here, h is the water depth, H_s is the infragravity significant wave height, T_w is the infragravity wave period, $\gamma = H_s/h$, and H_s/λ is the wave steepness.

Authors (Year)	h (m)	H_s (m)	T_w (s)	γ	H_s/λ
Sous et al. [55]	1.5	0.180–0.300	25–250	0.12–0.20	3.1×10^{-4}–1.9×10^{-3}
Masselink et al. [56]	0.5	0.060	-	0.12	-
Buckley et al. [2]	0.1	0.006–0.008	27–100	0.06–0.08	8.5×10^{-5}–2.4×10^{-4}

Table 1. *Cont.*

Authors (Year)	h (m)	H_s (m)	T_w (s)	γ	H_s/λ
Pomeroy et al. [57]	2.1	0.080–0.200	25–250	0.03–0.10	1.8×10^{-4}–7.1×10^{-4}
Beetham et al. [58]	1.2–2.0	0.100–0.400	>25	0.08–0.20	1.2×10^{-3}–3.6×10^{-3}
Cheriton et al. [3]	1.8–2.2	0.250–0.800	25–250	0.14–0.36	6.8×10^{-4}–2.4×10^{-3}
Van Dongeren et al. [26]	1.0	0.180–0.200	25–600	0.18–0.20	1.1×10^{-4}–2.3×10^{-3}
Pomeroy et al. [29]	1.5–1.8	0.040–0.080	100	0.03–0.04	1.0×10^{-4}–1.9×10^{-4}

The model domains were designed as two-dimensional reef flat profiles ranging in across-shore lengths of 144, 235, and 564 m, with a height of 2 m, the still water line centered at zero, and a constant depth of 1 m. Model domain lengths varied with the IG wavelength (λ = 94, 157, and 376 m) to ensure an entire wave was captured in each domain. The domains began with a region equal to one-half wavelength with a smooth bottom to initialize conditions, followed by a region equal to one whole wavelength containing the roughness elements, which were repeated at regular intervals from x = x_0 to x = L_m (Figure 1), where x is the across-model length in meters and L_m is the model domain length. Bed roughness was modeled with regular arrays of hemispherical objects with a constant diameter d = 0.4 m and height h_c = 0.2 m. Hemispheres were chosen for simplicity as these approximate the shape of robust corals such as *Porities*, *Diploastrea*, *Orbicella*, *Montastraea*, and *Siderastrea* genera that are increasingly being outplanted [59] as well as artificial structural reef elements such as the *ReefBall*^{TM}. The roughness density in the model domains varied with the across-shore distance between adjacent elements, D (Figure 1e). The final model scenarios combined one of six roughness densities: D = 2, 3, 4, 8, 16, and 32; with three incident wave heights: H_s = 0.05, 0.15, and 0.3 m; and three incident wave periods: T_w = 30, 60, and 120 s; for a total of 54 scenarios. These combinations of model scenarios simulated correspond to offshore wave heights H_0 of 1–5 m, offshore wave periods T_0 of 4–25 s, and reef flat widths W_f of 100–500 m (Table 2) based on the BEWARE database [8].

Table 2. Extrinsic offshore oceanographic conditions and intrinsic reef parameters in the BEWARE database [8] that correspond to the cases simulated in this study. Here, h is the water depth, H_{s0} is the infragravity wave height, and T_w is the infragravity wave period on the reef flat, H_0 is the wave height, T_0 is the wave period offshore, and W_f is the reef flat width for a given set of offshore conditions.

h (m)	H_{s0} (m)	T_w (s)	H_0 (m)	T_0 (s)	W_f (m)
1	0.05	30	1	5	350
1	0.05	60	4	7	150
1	0.05	120	1	11	400
1	0.15	30	2	10	500
1	0.15	60	1	6	250
1	0.15	120	3	25	500
1	0.30	30	5	16	100
1	0.30	60	5	5	250
1	0.30	120	3	11	150
1	0.60	120	4	23	500
1	0.60	360	1	9	150
1	0.60	720	1	11	200
1	0.90	120	3	4	200
1	0.90	360	2	5	500
1	0.90	720	1	4	200

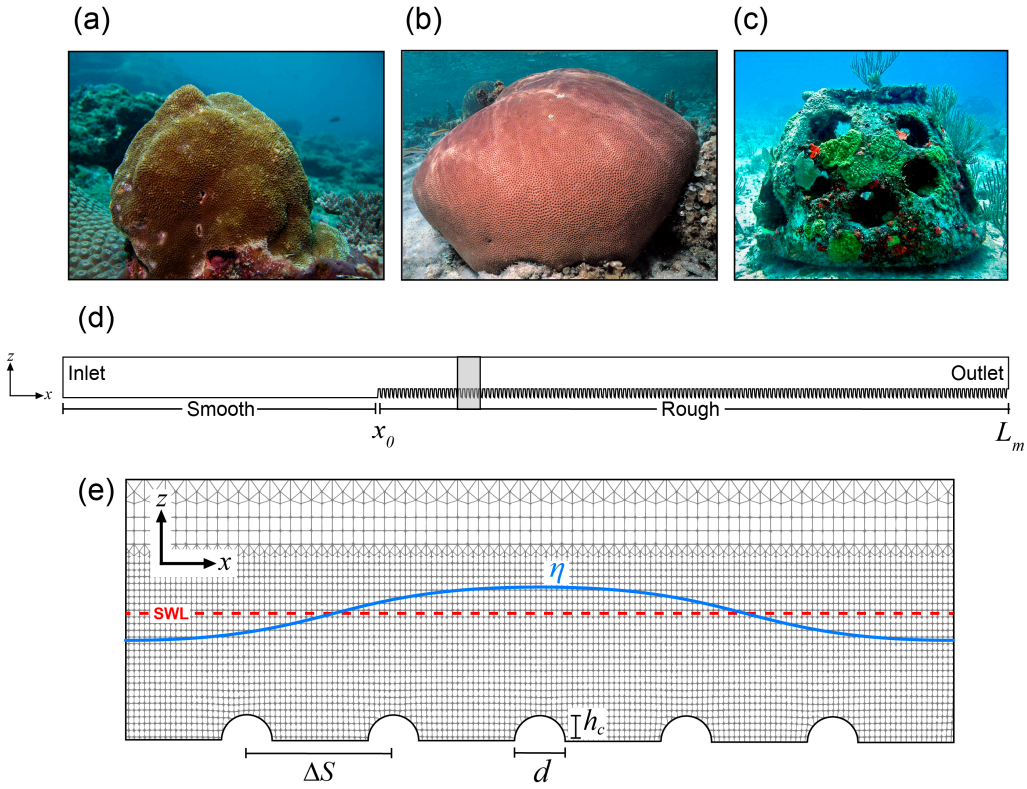

Figure 1. Coral reef hemispherical element examples and model setup. (**a**) Pacific *Porites solida*. (**b**) Caribbean *Siderastrea siderea*. (**c**) A *ReefBall*^{TM} encrusted with juvenile corals. (**d**) Full-scale model layout with vertical exaggeration to depict roughness. All models started with a smooth region equal to one-half wavelength, followed by a region between x_0 and L_m containing roughness equal to one whole wavelength. The approximate location of the enlarged schematic layout in (**e**) is depicted with a shaded rectangle in (**d**). Degrees of roughness were created by varying the across-shore spacing of elements $D = \Delta S/d$. In this figure, the still water line (SWL) is denoted as a dashed red line and the water surface elevation η as a solid blue curve. The wavelength has been shortened for illustrative purposes. In (**e**), the mesh refinement for the models is shown in the background. Photo credits: (**a**) Turak and Lyndon DeVantier, (**b**) Mary Stafford-Smith, (**c**) Reefball.org.

Despite the apparent similarity of the experimental design with studies of Bragg reflection (e.g., [60]), we note that the term $2\Delta S/L$ is between 0.004 and 0.273 for the conditions considered in this study, and hence Bragg reflection (which is maximum at $2\Delta S/L = 1$) is not one of the dominant processes studied here.

2.3. Numerical Model Set-Up

All models described herein used the same set-up and configuration as the calibrated and validated models described in Norris et al. [61]. Below we provide a brief description of the model set-up, but please refer to Norris et al. [61] for further details.

All model domains were quasi-two-dimensional (i.e., varying dimensions along the x and z axes with the y-axis defined as a single cell layer). Initial tests for grid cell independence were determined by first running a series of empty tank wave models without turbulence and with increasing grid resolution for each set of wave conditions to determine the resolution at which (i) wave heights did not decay with distance along the x-axis of the numerical wave flume, and (ii) the space-averaged (i.e., between x_0 and L_m; Figure 1) water velocity profiles converged. After choosing an appropriate resolution, the same exercise was repeated with turbulence activated to check the space-averaged turbulence profiles. The finest grid resolution was chosen for all wave conditions and was conservative for the largest waves. Hence, all domains started with a constant ($x = z$) mesh size of 0.2 m. Then, 3D STL models of the roughness elements (hemispheres) for each model domain

were created in Blender, and were placed inside the model domains to be 'snapped' to the bottom of the domains using the *snappyHexMesh* utility in OpenFOAM. Mesh refinement was conducted in three levels down to 0.025 m (Figure 1e). At the bottom of the models, this mesh scaling corresponded to dimensionless wall distances (z^+) of 50–150, where $30 < z^+ < 300$ defines the log-law layer where wall functions are applicable.

All models employed the following boundary conditions. The model inlet and outlet were set to *waveVelocity* for wave generation and absorption, respectively. The bottom wall and roughness elements used the *zeroGradient* condition, and the top of the model the *inletOutlet* condition. At the model inlet, outlet, and along the bottom, the *fixedFluxPressure* condition was applied to the hydrostatic field (pressure) to adjust the pressure gradient so that the boundary flux matched the velocity boundary condition. Active absorption was turned on at the inlet and outlet to reduce wave reflections inside the model domains. Turbulence was simulated using the *k*-ε model using a RANS approach. Since two-equation turbulence models are known to cause over-predicted turbulence levels beneath waves in numerical wave flumes, we stabilized the models using the method developed by Larsen and Fuhrman [62] using their default parameter values for the *k*-ε closure scheme.

Model turbulence parameters used respective wall functions to model the boundary layer profile near the bed. Initial values of the turbulence fields were specified using standard equations with $C_\mu = 0.09$, turbulent intensity of 5%, depth-averaged velocity from the empty wave tank models, and turbulent length scale set by the still water depth above the roughness elements. Cnoidal waves with IG frequencies were generated in the models using the IHFOAM toolbox [63]. All models were sampled at 12 Hz.

Sampling was conducted during model runtime for the area encompassing the free surface to the bed within the region of the model domain containing the roughness elements. Data analysis was conducted on the last ten waves in each scenario. Longer time series were also investigated, but initial testing revealed little difference in the results between these and shorter time series, due to the simulated waves being monochromatic. Given that simulation times varied between 2.5 to 37.5 h, depending on the model domain length and wave period, preference was given for shorter runtimes that achieved the same result as longer runtimes.

2.4. Model Data Analysis

The significant IG wave height, H_s was computed from the free surface time series of each model simulation as:

$$H_s(x) = 4\sqrt{\int S_\eta(x)\mathrm{d}f} \tag{1}$$

where $S_\eta(x)$ is the water surface elevation spectrum, which was estimated with Welch's method and a Hamming window, and $\mathrm{d}f$ is the step-in frequency. Estimates of H_s were computed at the positions x_0 and L_m (Figure 1d) to assess the change in wave height across each of the models.

To compare wave energy dissipation within the models, the change in the one-dimensional wave energy flux for shore-normal waves was computed as:

$$\frac{\partial F_j}{\partial x} = -\varepsilon_{b,j} - \varepsilon_{f,j} \tag{2}$$

where F_j is the wave energy flux across the model domain, $\varepsilon_{b,j}$ is the wave dissipation due to wave breaking, $\varepsilon_{f,j}$ is wave dissipation due to bottom friction, and the subscript j indicates the jth frequency component of a spectral wave distribution [31]. In general, F_j at any across-shore location is given by $F_j = E_j C_{g,j}$, where E_j is the wave energy and $C_{g,j}$ is the group velocity for a given spectral frequency. Here, we modeled only IG wave frequencies, as SS waves are often a negligible component of the total wave energy on reef flats far from the reef crest [29]. As none of the conditions modeled here induced wave breaking, Equation (2) can be simplified to:

$$\frac{\partial F_j}{\partial x} = -\varepsilon_{f,j} = -\frac{1}{4}\rho f_{e,j} u_{b,r} {u_{b,j}}^2 \quad (3)$$

where $f_{e,j}$ is the frequency-dependent energy dissipation factor, $u_{b,r}$ is a representative near-bottom wave orbital velocity, given by:

$$u_{b,r} = \sqrt{\sum_{j=1}^{N} {u_{b,j}}^2} \quad (4)$$

and $u_{b,j}$ is the velocity corresponding to the jth frequency component [31]. The mean wave orbital excursion A_b was estimated from the mean value of $u_{b,r}$ and T_w as $A_b = u_{b,r} T_w / 2\pi$ for each model scenario. $u_{b,j}$ was estimated from the water surface elevation spectrum ($S_{\eta,j}$) using linear wave theory:

$$u_{b,j} = \frac{a_j \omega_j}{\sinh k_j h} \quad (5)$$

where k_j is the wavenumber, ω_j the wave radian frequency ($= 2\pi f$), and the wave amplitude is $a_j = \sqrt{2 S_{\eta,j} \Delta f}$, with Δf the spectral bandwidth. In Section 3.2, F_j is presented at a single incident wave height for three incident wave periods and two across-shore element spacings. Equations (3)–(5) were used to estimate $f_{e,j}$ to assess frequency-dependent wave dissipation across the model domains from x_0 to L_m.

To compare wave-frequency velocity attenuation within the canopy layer of the models, we define the wave attenuation parameter per unit frequency $\alpha_{w,j}$ as

$$\alpha_{w,j} = \left(\frac{\hat{S}_{U,j}}{S_{U,j}} \right)^{1/2} \quad (6)$$

where $\hat{S}_{U,j}$ is a depth-averaged velocity spectrum assessed within the canopy layer near the bed in the models, and $S_{U,j}$ is a depth-averaged velocity spectrum assessed just below the free surface [46]. To estimate $\alpha_{w,j}$, we used depth-averaged velocities from four vertical cells at each position: within the canopy layer (z = 0.8–0.90 m) and below the free surface (z = 0.1–0.2 m). Spectra were calculated with a Hamming window and 50% overlap to yield approximately 20 DOF.

The total energy dissipation in the models was assessed using the TKE dissipation rate (ε) calculated by OpenFOAM in each model grid cell. To simplify the model results, ε was binned along the x-z plane into 26 vertical (z) bins and between 1008 and 3984 horizontal (x) bins to keep the horizontal bin size consistent between model domains with different lengths. The binned estimates of ε were then time-averaged to produce a representation of the mean conditions for each model scenario. ε results are presented both in terms of depth-averaged with respect to the across-shore distance (x) in the models x/L_m, space-averaged with respect to depth (z), and depth-and-space averaged to compare with the number of elements per meter, n.

Finally, model performance in wave height reduction and energy dissipation is quantified as the percent change in these parameters across the models for each scenario, and was estimated as $Percent\ Change = \frac{\beta_{L_m} - \beta_{x_0}}{\beta_{x_0}} \cdot 100$, where β is H_s or depth-averaged ε, β_{x_0} is the parameter value at the beginning of the bottom roughness, and β_{L_m} the value at the end. Greater negative values represent a larger percent change in each parameter for each model scenario.

3. Results

3.1. Infragravity Wave Attenuation

As IG waves propagate across the model domains, they are gradually attenuated as near-bed wave velocities are converted into turbulence. Raw output from the models demonstrates this conversion of wave energy above and within the hemisphere canopy

(Figure 2). The greatest velocities occur under the wave crests, with larger accelerations along the top of the roughness elements (Figure 2a). Velocity shadows in the lee of the elements are indicative of eddying that drives turbulent energy dissipation. Accordingly, greater turbulence is concentrated beneath the wave crest where velocities are intensified, although high turbulence can also be observed downstream of the wave crest at the top and in between the roughness elements (Figure 2b).

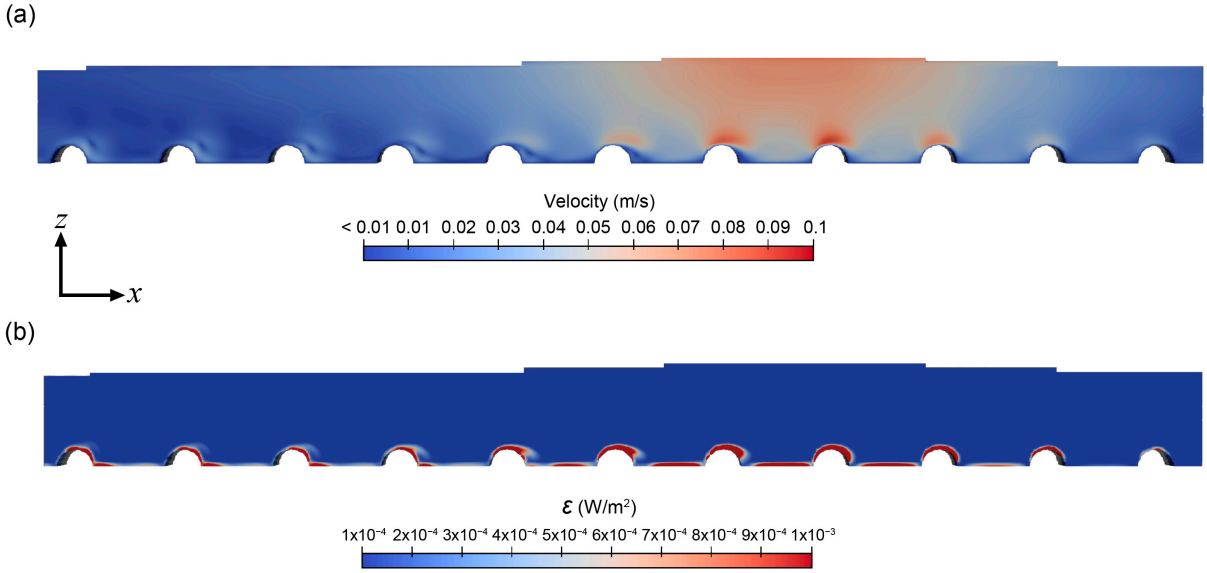

Figure 2. Example model output (a single timestep) depicting an infragravity wave crest passing over the bottom roughness from a model with water depth, h = 1 m, wave height, H_{s0} = 0.05 m, wave period, T_p = 30 s, and element spacing, D = 3. In the figure, the wave propagates from left (offshore) to right (onshore). (**a**) Velocity magnitude. (**b**) Turbulent kinetic energy (TKE) dissipation rate, ε. Low parameter values are in blue and high values in red. The velocity magnitude demonstrates accelerating water at the top of the roughness elements and decelerating water in the wake of individual elements. These accelerations and decelerations generate turbulence above and behind the elements.

The percent change in H_s across the models depends on the incident IG wave height H_{s0}, the wave period T_w, and element spacing D, with greater attenuation for shorter element spacings, larger waves, and longer wave periods (Figure 3). For any T_w, the difference between the D = 2 and 32 roughness element spacings also grows with increasing H_{s0}.

Changes in wave energy flux across the model domains are dependent on incident wave conditions. In general, the wave energy flux spectra (F_j) decrease from the beginning (x_0) to the end (L_m) of the roughness, with increasing T_w and D at constant H_{s0} (Figure 4). For the D = 2, T_w = 30 s case (Figure 4a), the decrease in wave energy occurs mainly between the incident frequency f = 0.035 and 0.23 Hz, and wave energy above f > 0.23 Hz shows little decrease from x_0 to L_m. In contrast, wave energy in the D = 32, T_w = 30 s case (Figure 4b) is dissipated mainly at higher frequencies, f = 0.08 and 0.33 Hz, with more energy remaining at L_m at the incident frequency. A similar pattern repeats for the T_w = 60 and 120 s models (Figure 4c–f). Thus, dense bed roughness more efficiently removes energy from the waves as it acts on both the incident and higher frequencies, regardless of the incident wave period. Sparse bed roughness is less effective at removing wave energy as it acts mainly on higher frequencies.

Indeed, spectra of the energy dissipation factor $f_{e,j}$ (Equation (3)) for the same cases shown in Figure 4a,b demonstrates that the majority of wave dissipation in the D = 2 case occurs at approximately the predominant frequency f_j = 0.035 Hz (T = 29 s), but occurs at higher frequencies f_j = 0.13 Hz (T = 8 s) in the D = 32 case (Figure 5). Similarly, spectral decomposition of near-surface S_U and in-canopy velocities $\hat{S}_U$ for the same cases indicate

that in-canopy velocities are severely reduced at the predominant frequency in the $D = 2$ case (Figure 6a) yet are minimally reduced in the $D = 32$ case (Figure 6b). Consequently, $\alpha_{w,j}$ is lowest close to the predominant frequency for the $D = 2$ case (Figure 6c) and remains $\alpha_{w,j}$~1 across almost all frequencies for the $D = 32$ case (Figure 6d). These results indicate that the $D = 2$ model efficiently attenuates wave velocities at the predominant frequency, whereas the $D = 32$ model is much less efficient at dissipating energy at the predominant frequency.

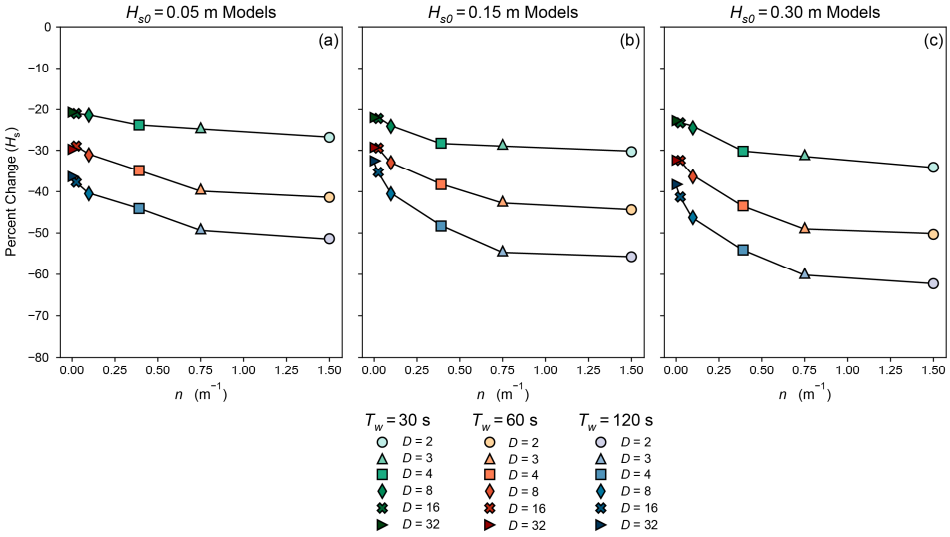

Figure 3. Percent change in modelled wave height H_s across the roughness versus the number of elements per across-shore meter n, for three wave periods, T_w = 30 s, 60 s, and 120 s (colors); three incident wave heights, H_{s0} = 0.05 (**a**), 0.15 (**b**), and 0.30 m (**c**); and six across-shore element spacings, D = 2–32 (shapes). Wave height decreases with increasing across-shore element spacing for all model scenarios, with greater wave attenuation for closer element spacings and larger waves.

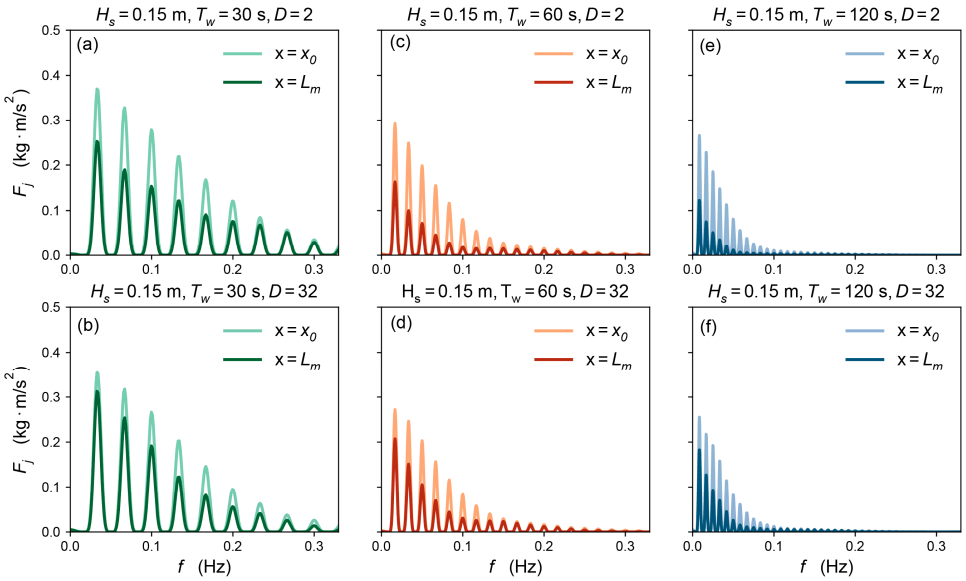

Figure 4. Spectra of wave energy flux (F_j) across different wave frequencies (f_j) for a single wave height (H_{s0} = 0.15 m), and three incident wave periods T_w = 30 s (**a**,**b**), 60 s (**c**,**d**), and 120 s (**e**,**f**), for the smallest (D = 2) and largest (D = 32) across-shore element spacings. Power spectra are shown for the beginning (x_0) and end (L_m) of the simulated roughness. Loss of wave energy occurs at the predominant frequency for restorations with short element spacings (D = 2), and at higher frequencies for larger spacings (D = 32). Hence, denser restorations dissipate wave energy more efficiently than sparser restorations.

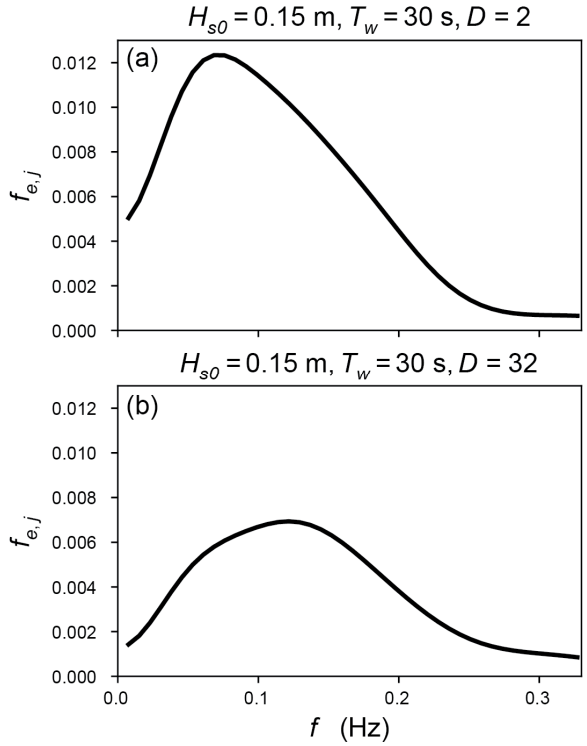

Figure 5. Wave energy dissipation factor $f_{e,j}$ as a function of frequency, calculated from the wave energy flux and near-bottom wave-orbital velocity using linear wave theory (Equation (3)) for two cases, H_{s0} = 0.15 m, T_w = 30 s and two across-shore element spacings D = 2 (**a**) and D = 32 (**b**). These values correspond to the energy flux spectra shown in Figure 4a,b. For the D = 2 case, $f_{e,j}$ is greatest around the predominant frequency f_j = 0.035 Hz. Conversely, for the D = 32 case, $f_{e,j}$ is greatest at higher frequencies, f_j = 0.13 Hz.

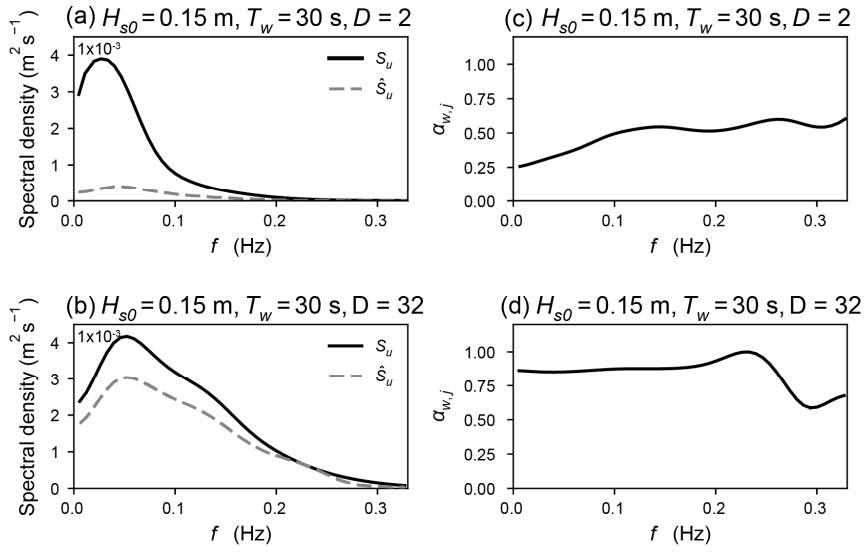

Figure 6. Spectra of wave energy attenuation parameters for two cases, H_{s0} = 0.15 m, T_w = 30 s and two across-shore element spacings D = 2 and 32. (**a**,**b**) Decomposition of the velocity spectrum above the canopy S_u and velocity spectrum within the canopy layer $\hat{S}_u$ for two cases, H_{s0} = 0.15 m, T_w = 30 s and two across-shore element spacings D = 2 and 32. (**c**,**d**) Spectral wave attenuation parameter $\alpha_{w,j}$ as a function of frequency (Equation (6)). When canopy elements are densely spaced (**a**,**c**), in-canopy velocities are highly attenuated by drag. When elements are sparse (**b**,**d**), in-canopy velocities are hardly attenuated and $\alpha_{w,j}$~0.8 across most frequencies.

3.2. Dependence of Turbulence on Bottom Roughness

Normalized across-shore profiles (x/L_m) of the depth-averaged TKE dissipation rate (ε) for every model scenario demonstrate that ε decreases with increasing T_w and D, and increases with increasing H_{s0} (Figure 7). The decline of ε in the across-shore direction is generally monotonic for almost all models. However, models with dense element spacings (i.e., D = 2 to 4) have an inflection point around half the model domain length (x/L_m = 0.5) where the rate of change in ε decreases (for example, this pattern is especially apparent in the D = 2 case with H_{s0} = 0.30, T_w = 120 s, Figure 7i). However, this inflection point becomes less obvious as the element spacing increases. One possible explanation for this behavior is that a wave will encounter more elements when they are spaced closer together, resulting in greater initial energy dissipation that weakens with cross-shore distance. Interestingly, although the T_w = 30 s models also exhibit a decline in energy dissipation across the models for shorter element spacings, there is a nearly constant dissipation with cross-shore distance for larger element spacings (e.g., compare D = 2 to D = 32 in Figure 7c).

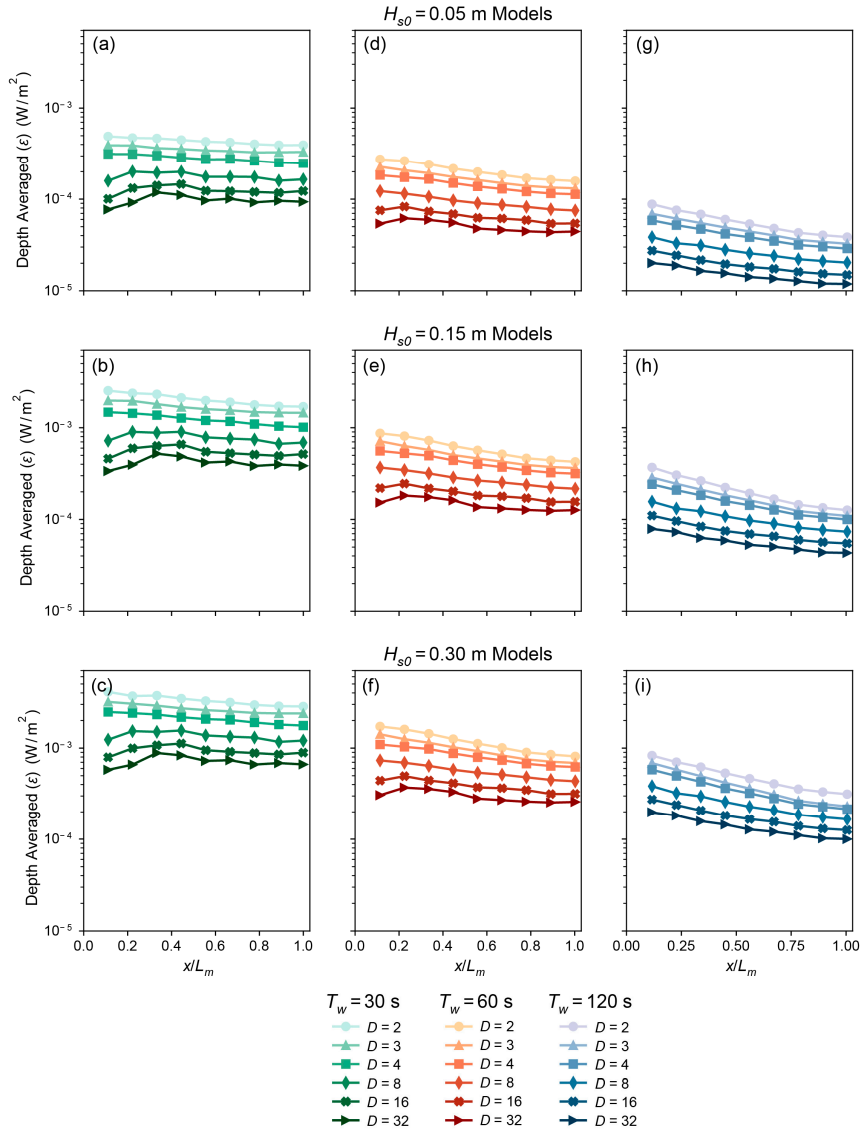

Figure 7. Points of depth-averaged turbulent kinetic energy (TKE) dissipation (ε) at even positions within the roughness elements for three wave periods T_w = 30 s (**a–c**), 60 s (**d–f**), and 120 s (**g–i**); three incident wave heights H_{s0} = 0.05 (**top** row), 0.15 (**middle** row), and 0.30 m (**bottom** row); and six across shore element spacings D = 2–32 (shapes). ε increases with incident wave height and decreases with increasing wave period and element spacing.

Time-and-space averaged depth profiles of ε (Figure 8) reveal increasing variance in the vertical distribution of turbulence under increasing wave heights and periods. Under the smallest IG waves (H_{s0} = 0.05 m), ε is enhanced only for the D = 2 cases, with peak ε occurring below the top of the roughness elements around z = 0.9 m depth. Similar to the across-shore profiles (Figure 7), this peak ε tends to decrease with increasing T_w at constant H_{s0}, from a maximum of 9 × 10^{-4} W/m^2 under T_w = 30 s waves (Figure 8a) to a maximum of 1 × 10^{-4} W/m^2 under T_w = 120 s waves (Figure 8g). As the incident wave height increases, enhanced ε also occurs in the D = 3 and D = 4 cases, with a greater distribution of ε higher in the water column above the roughness elements (Figure 8b,e,f). Finally, under the largest wave conditions, enhanced ε within and above the canopy layer is observed for the D = 2 to 8 cases, particularly for the T_w = 120 s models (Figure 8c,f,i).

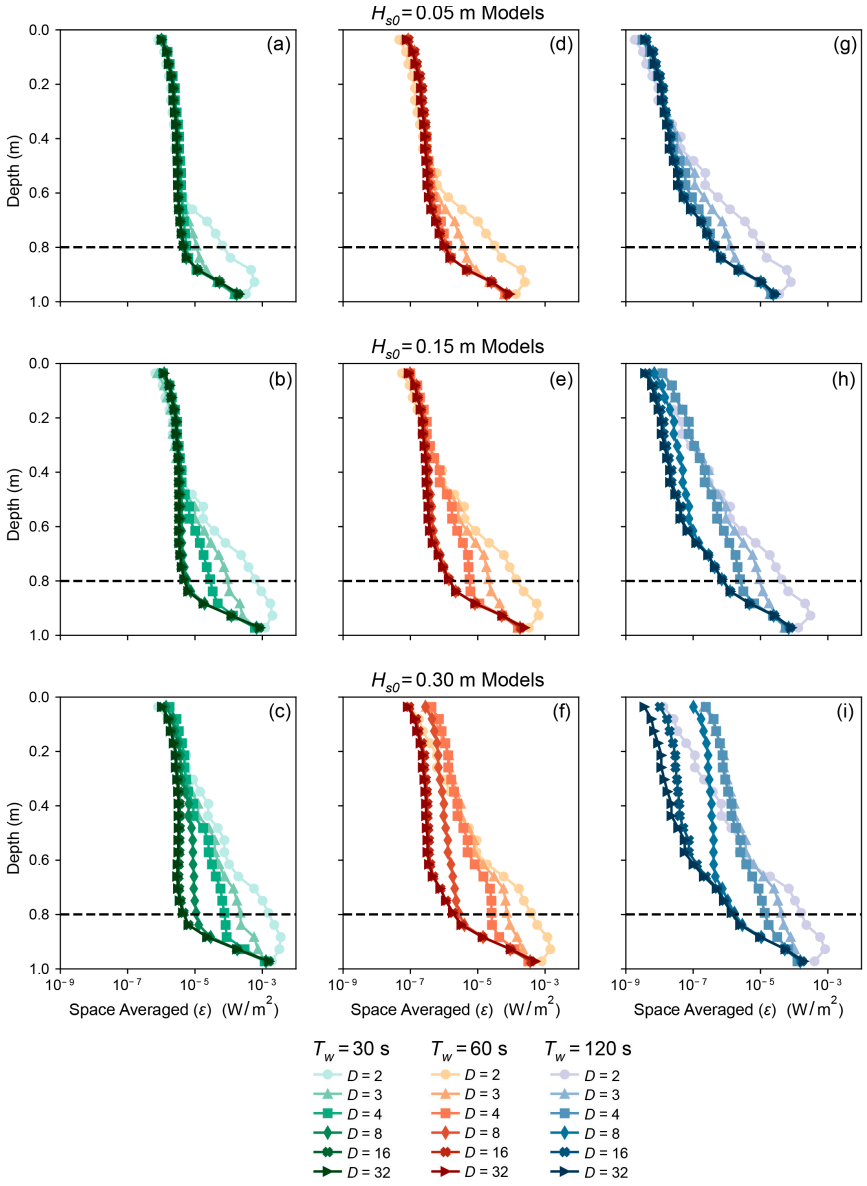

Figure 8. Depth profiles of the turbulent kinetic energy (TKE) dissipation rate (ε) averaged across the roughness elements for three wave periods T_w = 30 s (**a–c**), 60 s (**d–f**), and 120 s (**g–i**); three incident wave heights H_{s0} = 0.05 (**top** row), 0.15 (**middle** row), and 0.30 m (**bottom** row); and six across-shore element spacings D = 2–32 (shapes). The dashed black line denotes the top of the reef elements in each subplot. As in Figure 7, turbulence increases with decreasing spacing and increasing incident wave height. Greater turbulence occurs higher in the water column under larger waves with smaller element spacings and is principally concentrated near the bed with larger element spacings.

Like the other turbulence metrics (Figures 7 and 8), the depth-and-space averaged value of ε for each model scenario increases with H_{s0}, and decreases with T_w, n, and D (Figure 9). There is an inflection point on the curves of n and ε, where ε is nearly constant for further reductions in n (Figure 9). This inflection point occurs at much larger n for small incident waves (H_{s0} = 0.05) and at smaller n as the incident wave height increases. Critically, these inflection points represent the maximum energy dissipation attained for a minimum number of restoration elements. This result also reveals an equivalency between different roughness densities under varying wave conditions: smaller incident waves passing over a denser canopy of restoration elements can produce similar levels of energy dissipation as larger waves passing over a sparser canopy of elements.

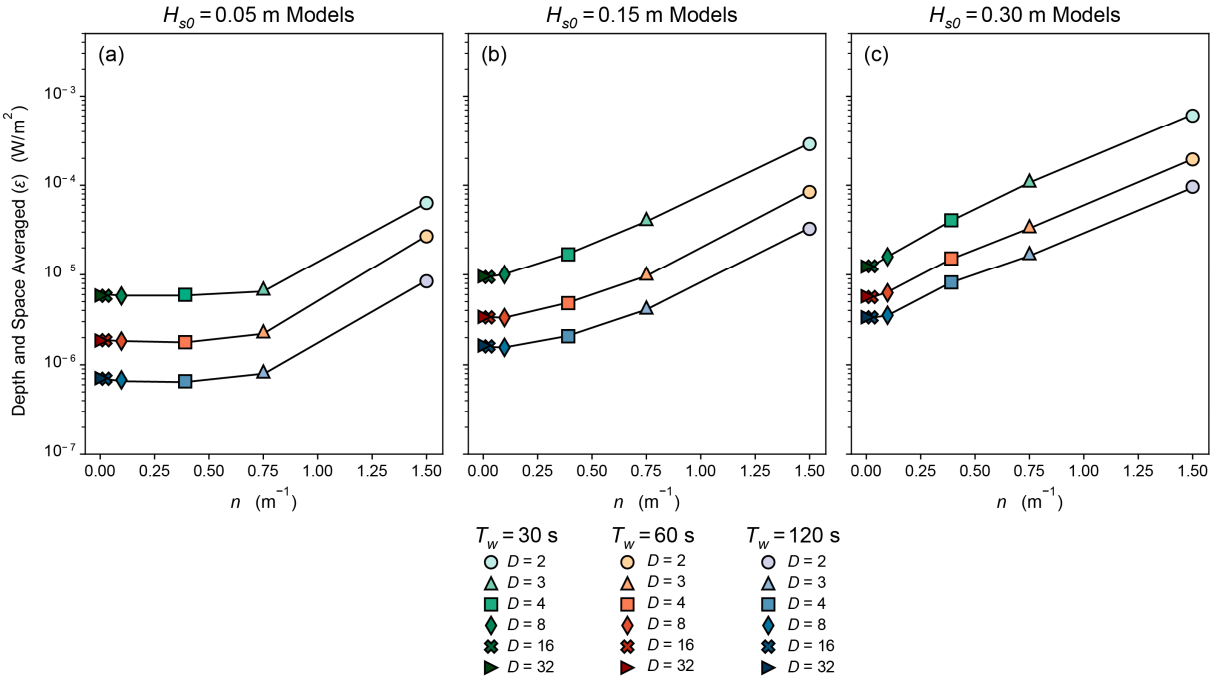

Figure 9. The depth and space averaged turbulent kinetic energy (TKE) dissipation rate (ε) against the number of elements per across shore meter (n) for three wave periods T_w = 30–120 s (colors); three incident wave heights H_{s0} = 0.05 (**a**), 0.15 (**b**), and 0.30 m (**c**); and six across-shore element spacings D = 2–32 (shapes). In general, ε decreases with n (and D), starting from a maximum value at D = 2 for all cases. The inflection point of these curves is a key balance point between TKE dissipation and element spacing, representing the restoration design that maximizes dissipation while minimizing the number of restoration elements, and hence the potential cost of the restoration, for each set of incident wave conditions.

However, increasing incident wave conditions does not always result in greater energy dissipation, as identified by the percent change in ε (Figure 10). Increases in H_{s0} from 0.05 to 0.15 m result in a greater change in energy dissipation, which also negatively scales with n (and D), and positively with T_w. Further increases in H_{s0}, from 0.15 to 0.30 m, result in a smaller change in energy dissipation, with minimal improvements for only the densest canopy spacings (see D = 2 through D = 4 in Figure 10b,c). This result indicates there are diminishing returns in energy dissipation with respect to wave conditions and canopy density.

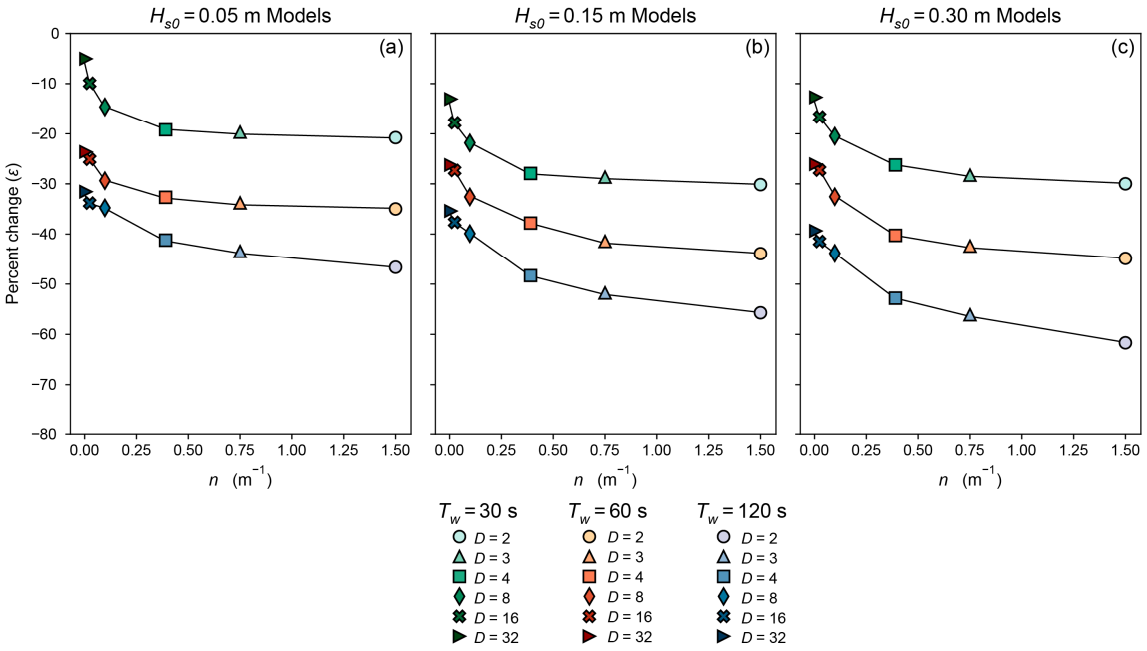

Figure 10. The percent change in depth and space averaged turbulent kinetic energy (TKE) dissipation rate (ε) against the number of elements per across shore meter (n) for three wave periods T_w = 30–120 s (colors); three incident wave heights H_{s0} = 0.05 (**a**), 0.15 (**b**), and 0.30 m (**c**); and six across-shore element spacings D = 2–32 (shapes). The change in ε increases with n across all cases, however the greatest change was observed for T_w = 120 s waves. There is a noticeable change in ε between H_{s0} = 0.05 and 0.15 m, and negligible change between H_{s0} = 0.15 and 0.30 m. Hence, improvements in ε may not be achievable by increasing element density beyond certain limits.

4. Discussion

This study considered IG wave dissipation across a schematic reef flat with varying, uniform across-shore spacings of structural reef elements. We simulated coral reef roughness using idealized hemispherical forms, using a similar approach as other physics-based investigations of wave interactions with large roughness elements (e.g., [44,45]). These forms are a simplification of real reef bathymetry but approximate the shape of certain coral genera, as well as commercial artificial reef elements. The model results demonstrated that IG wave energy dissipation is enhanced both in the horizontal dimension (across-shore) and the vertical dimension (within the water column) when incident waves are large and wave periods are small (Figures 7 and 8). For smaller waves (H_{m0} = 0.05 m in our experiments), frictional dissipation rolls off towards nearly a constant value as the roughness spacing drops below D = 3, and similar patterns were only observed for larger waves when the roughness spacing was considerably greater (Figure 9), reminiscent of results obtained by Buccino et al. [64] for their work on *ReefBall*^{TM}-assisted wave attenuation.

With respect to coral reef restoration design, there are several important considerations with the findings in the present work: (1) wave dissipation is not constant across all frequencies and varies with canopy density; (2) there are diminishing returns in dissipation with increasing wave height and canopy density; and (3) an efficient restoration design is one that generates maximal wave energy dissipation using a minimum number of canopy elements. Not only will this strategy minimize the cost of a restoration project but may also be beneficial when wave heights above the restoration area increase during storm conditions, as explained below.

4.1. Wave-Frequency Dissipation

The results demonstrated that wave energy dissipation is not constant across all frequencies and depends on both the incident wave conditions and the roughness density. This topic has been the focus of several pivotal studies in wave-canopy flow dynamics [31,46,65,66].

Theory from Lowe et al. [46] predicts the wave attenuation parameter $\alpha_{w,j}$ will be large when canopy density is small relative to the length scale of bed roughness, k_w. Using linear theory to estimate the near-bottom velocity for the cases presented in Figure 5 yields A_b on the order of 11 m for the D = 2 case, and 18 m for the D = 32 case. If we take k_w as ΔS for these cases, then $A_b/k_w > 1$ for the D = 2 case and $A_b/k_w < 1$ for the D = 32 case. From this exercise, it follows that $\alpha_{w,j}$ should be small for the D = 2 case, when velocity reduction is greatest, and large for the D = 32 case, when velocity reduction is smallest (Figure 6c,d). A similar pattern follows for $f_{e,j}$ (Figure 5), except that estimates presented for the D = 32 case may be larger than in actuality. When $A_b/k_w \leq 1$, inertial forces dominate canopy flow [46]. Since the inertial force is in quadrature with the water velocity and does no work, friction factors determined with Equation (3) likely overestimate the true value in this case [45]. Regardless, this reinforces the idea that a dense canopy is much more efficient in removing wave energy at the dominant frequency than a sparse canopy.

4.2. Diminishing Returns in Wave Dissipation

Another interesting finding is that increasing the roughness density of the seabed through restoration may not always lead to further increases in wave energy dissipation. Although the greatest energy dissipation was observed for the densest canopies under the largest waves (Figure 9c), the percent change in dissipation diminished as the incident wave height increased (Figure 10). Hence, utilizing a lower coral density design could be more beneficial because it could greatly enhance energy dissipation as incident wave heights increase (as demonstrated between the H_{s0} = 0.05 and 0.15 m cases in Figure 10).

This effect of diminishing returns in wave dissipation can be explained by a simple model for wave dissipation based on a standard drag coefficient model for canopy friction [65]. The damping of wave velocities within bottom roughness is governed by the dimensionless damping parameter $\Lambda_0 = C_D a|u_b|T_w/4\pi$, where u_b is the near-bottom velocity, C_D is the canopy drag coefficient, and the hemisphere frontal area is $a = (1/8)\pi d^2$. Theory predicts when Λ_0 = 1.4, in-canopy velocities are substantially reduced by drag and wave dissipation is maximized. Dissipation rolls off either when $\Lambda_0 << 1$, because in-canopy velocities are minimally reduced by drag forces, or when $\Lambda_0 >> 1$, because in-canopy velocities decline nearly to zero. For the two cases presented in Figure 5, we estimate C_D (as the total drag coefficient calculated by OpenFOAM for each scenario) as 0.26 for the D = 2 case and 0.25 for the D = 32 case. These C_D values are generally consistent with those estimated by Yu et al. [45] in a similar modeling study of idealized, hemispherical bottom roughness. For the two cases presented in Figure 5, we estimate Λ_0 = 1.766 and 0.006 for the D = 2 and D = 32 cases, respectively, reiterating that energy dissipation is more efficient within a denser canopy for the incident wave conditions (recalling these are H_{s0} = 0.15 m and T_w = 30 s). This result also demonstrates that the D = 2 case is already close to maximum dissipation at Λ_0 = 1.4. A doubling of wave height to H_{s0} = 0.30 m would yield Λ_0 = 2.854 and 0.011 for the D = 2 and 32 cases, indicating that dissipation would decrease within the D = 2 canopy, suggesting no increased benefit could be achieved with such dense element spacing given these conditions. The use of a more moderate spacing, such as the 'inflection point spacing' identified in Figure 9, would allow for enhanced dissipation to occur if wave conditions became more intense during storm conditions.

4.3. Cost Implications in Optimizing Reef Restoration Design

For a given set of wave conditions, there is an optimal spacing of roughness elements that balances wave energy dissipation with element spacing (Figure 9). The relationship between the percent change in energy dissipation and the number of roughness elements per across-shore meter n is inversely related, such that similar levels of wave energy dissipation can be achieved with larger n under smaller waves, or smaller n under larger waves (Figure 10). It is reasonable to assume that the cost of a potential restoration project also varies with n, and the cost is also proportional to incident wave conditions (Figure 11). How-

ever, many other factors affect the engineering design and cost of a restoration project [23] and additional work is necessary to determine the true shape of the 'cost curve'.

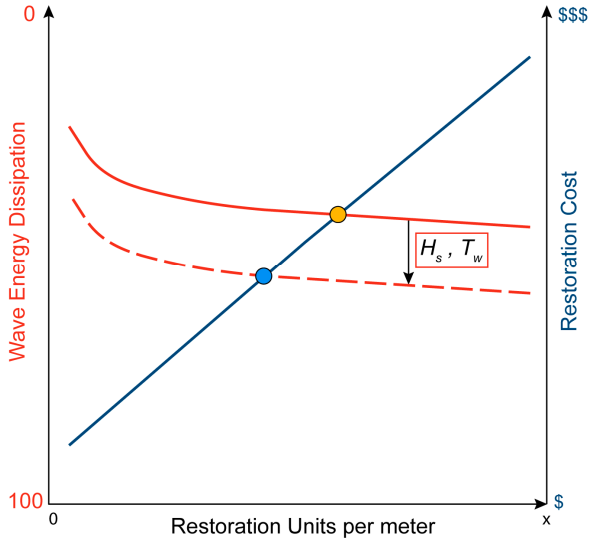

Figure 11. A schematic of percent change in energy dissipation (red curves, see Figure 10) versus the number of structural reef restoration elements per across-shore meter versus the hypothetical cost of restoration (blue line). Here, we represent the restoration cost (from lower cost, \$, to higher cost, \$\$\$) as a linear function of restoration unit numbers for simplicity. Percent dissipation increases as incident conditions (H_s, T_w) increase (from the solid to dashed red lines), necessitating fewer reef elements and lower cost, such that the price of the restoration moves from orange to blue circle on the cost curve and thus decreases.

4.4. Biological Implications in Optimizing Reef Restoration Design

In this paper, we demonstrated that the intensification of turbulence within and above a canopy of roughness elements depends both on the incident wave conditions as well as the canopy density. This interplay between restoration element spacing and wave energy dissipation likely has important biophysical implications that would affect the ability of a coral restoration to be biologically efficient and thus self-sustaining and self-propagating, along with providing coastal protection. As sessile, benthic organisms, corals depend on mass transfer from and to the overlying water to facilitate many biologically important processes, including mitigating thermal stresses via advective transport, nutrient exchange, coral heterotrophy, and larval dispersal and settlement [67]. Indeed, many biological processes vital to coral health depend on turbulence near the coral surface, as it drives in-reef circulation (see the recent review by Davis et al. [41]). For example, nutrient uptake in coral reefs is highly dependent on turbulent energy dissipation, with maximal uptake rates occurring in shallow systems with large bottom roughness elements [68]. Similarly, stronger flow may help to mitigate the effects of bleaching; Nakamura and Van Woesik [69] showed that coral bleaching at high water temperatures can be partially suppressed if turbulent boundary layer flows are strong. Besides the transfer of nutrients, turbulent mixing aids in reef heterotrophy and larval transport. Uptake rates of picoplankton by coral communities have been shown to increase relative to greater turbulent transport within coral canopies [70]. Through hydrodynamic modeling, Reidenbach et al. [71] demonstrated that the intensity of fluid forces on coral larvae depends on the degree of bathymetric roughness, with greater shear stresses for wider-spaced roughness than tightly spaced roughness. If shear stresses at the seabed are too intense, the larva can become detached from the benthos and may not be able to resettle.

Hence, there is likely an optimum spacing of roughness elements (coral communities) that will promote turbulent processes to enhance the biological processes of reefs. If roughness elements are too closely spaced, intensified turbulence may inhibit larval settlement. If

elements are too far apart, turbulent fluxes would be minimal and diminish mass transfer between adjacent elements (e.g., Figure 7). Another factor of the element spacing is the distribution of turbulence throughout the water column, where closer element spacings would likely result in greater mass exchanges to and from the canopy (e.g., Figure 8). Thus, balancing turbulence by optimizing element spacing would be a key step in maintaining the productivity of coral restorations and artificial reefs to ensure their health and hence their coastal defense capabilities.

5. Conclusions

Along coral fringing and atoll reef-lined coasts, low-frequency infragravity waves are often the primary driver of coastal flooding. Since recent research indicates that coral restorations on shallow reef flats may be most effective for reducing wave-driven runup and coastal flooding, this study of infragravity waves over-idealized hemispherical forms on shallow reef flats illustrates that the dynamics of wave-driven flow over high-relief topography are strongly dependent both on the incident wave conditions and the canopy density. As waves propagate over rough bathymetry, near-bed turbulence strips energy from the flows, which ultimately reduces wave height. Greater wave energy dissipation occurs for greater canopy density, larger infragravity wave heights, and shorter wave periods. Wave dissipation is also frequency-dependent: dense canopies are efficient in removing energy from waves at the predominant frequency, whereas sparse canopies are inefficient. This difference occurs due to a greater reduction in in-canopy wave velocities in dense canopies compared to sparse canopies. Larger wave heights and longer wave periods also generally increase the vertical distribution of turbulence within the water column above the canopy layer, as well as peak turbulence inside the canopy layer.

Collapsing dissipation estimates into a single, representative mean value for each model scenario demonstrated an 'inflection' or 'balance' point where enhanced dissipation is balanced by a minimum number of elements per across shore meter. Such balance represents the optimum canopy density to dissipate a given set of incident wave conditions. Although turbulent energy dissipation can be enhanced by either increasing canopy density for given wave conditions, or the incident wave conditions for a given density, there is a limit where further increases in either parameter leads to lower dissipation. These results, therefore, have implications for optimizing reef restoration design as projects could be designed with the best balance between costs and performance in terms of infragravity wave attenuation.

Restoration managers can use the results presented in this paper to design restoration studies that maximize IG wave energy dissipation for a minimum number of coral outplantings. Table 2 can be leveraged to determine the reef flat width and offshore wave conditions from the BEWARE database, and then the expected change in IG wave energy dissipation for a set number of restorations per across-shore meter is presented in Figure 10. We advise using a moderate number of restorations per across-shore meter as this will have a positive influence on IG wave dissipation across reef flats, while still reducing the total cost of the restoration project.

Author Contributions: Conceptualization, B.K.N., C.D.S. and A.W.M.P.; methodology, B.K.N. and C.D.S.; software, B.K.N.; validation, B.K.N.; formal analysis, B.K.N., C.D.S. and A.W.M.P.; investigation, B.K.N.; resources, C.D.S.; data curation, B.K.N.; writing—original draft preparation, B.K.N.; writing—review and editing, B.K.N., C.D.S., A.W.M.P. and B.G.R.; visualization, B.K.N.; supervision, C.D.S.; project administration, B.K.N. and C.D.S.; funding acquisition, C.D.S. All authors have read and agreed to the published version of the manuscript.

Funding: This project was funded by the U.S. Geological Survey Coastal and Marine Hazards and Resources Program, the U.S. Geological Survey Mendenhall Research Fellowship Program, and the Australian-America Fulbright Commission. B.G.R. was partly supported by an Early-Career Research Fellowship from the Gulf Research Program of the National Academies of Sciences, Engineering, and Medicine, although the content is solely responsibility of the author and does not necessarily

represent the official views of the Gulf Research Program of the National Academy of Sciences, Engineering and Medicine.

Institutional Review Board Statement: Not applicable.

Informed Consent Statement: Not applicable.

Data Availability Statement: The OpenFOAM model data sets analyzed in this manuscript are available from USGS ScienceBase.

Acknowledgments: The authors would like to thank Mark Buckley (USGS) and Stephen Henderson (Washington State University) for their helpful advice and guidance, as well as Babak Teranirad (USGS) for their peer review of an earlier version of this manuscript. Any use of trade, firm, or product names is for descriptive purposes only and does not imply endorsement by the U.S. Government.

Conflicts of Interest: The authors declare no conflicts of interest.

Nomenclature

A_b	wave orbital excursion
a	wave amplitude
C_g	wave group velocity
C_D	canopy drag coefficient
D	roughness element spacing
d	roughness element diameter
E	total wave energy
F	wave energy flux
f_e	wave energy dissipation factor
f	frequency
g	gravitational constant (=9.81 m/s^2)
H_{s0}	incident significant wave height
H_s	significant wave height
H_0	offshore significant wave height
h	water depth
h_c	roughness element height
IG	infragravity wave band
j	the j-th frequency component of a spectrum
k	wavenumber
k_w	bottom roughness
L_m	model wave flume length
n	number of roughness elements per across shore meter
r	a representative value
rms	root-mean-square
SS	sea-swell wave band
S_η	water surface elevation spectrum
$\hat{S}_U$	velocity spectrum within the roughness layer
S_U	velocity spectrum above the roughness layer
T_w	wave period
T_0	offshore wave period
u_b	near-bottom orbital velocity
U	velocity magnitude
W_f	reef flat width
x	across-shore distance in models
x_0	start of roughness elements in models
z	depth in models
z^+	wall distance function
α_w	canopy attenuation parameter (Lowe et al., 2005b)
Δf	spectral bandwidth
ΔS	center-to-center distance between adjacent roughness elements

Δx	model cell size in the direction of the velocity
ε	turbulent kinetic energy dissipation rate
ε_b	wave dissipation due to breaking
ε_f	wave dissipation due to bottom friction
γ	critical wave breaking parameter
κ_c	interface curvature (of the free surface)
Λ_0	wave damping parameter (Henderson et al., 2017)
λ	wavelength
ω	wave radian frequency
ρ	water density (=1025 kg/m^3)

References

1. Baldock, T.E.; Golshani, A.; Callaghan, D.P.; Saunders, M.I.; Mumby, P.J. Impact of Sea-Level Rise and Coral Mortality on the Wave Dynamics and Wave Forces on Barrier Reefs. *Mar. Pollut. Bull.* **2014**, *83*, 155–164. [CrossRef] [PubMed]
2. Buckley, M.L.; Lowe, R.J.; Hansen, J.E.; Van Dongeren, A.R.; Storlazzi, C.D. Mechanisms of Wave-Driven Water Level Variability on Reef-Fringed Coastlines. *J. Geophys. Res. Ocean.* **2018**, *123*, 3811–3831. [CrossRef]
3. Cheriton, O.M.; Storlazzi, C.D.; Rosenberger, K.J. Observations of Wave Transformation over a Fringing Coral Reef and the Importance of Low-Frequency Waves and Offshore Water Levels to Runup, Overwash, and Coastal Flooding. *J. Geophys. Res. Ocean.* **2016**, *121*, 3121–3140. [CrossRef]
4. Escudero, M.; Reguero, B.G.; Mendoza, E.; Secaira, F.; Silva, R. Coral Reef Geometry and Hydrodynamics in Beach Erosion Control in North Quintana Roo, Mexico. *Front. Mar. Sci.* **2021**, *8*, 684732. [CrossRef]
5. Ferrario, F.; Beck, M.W.; Storlazzi, C.D.; Micheli, F.; Shepard, C.C.; Airoldi, L. The Effectiveness of Coral Reefs for Coastal Hazard Risk Reduction and Adaptation. *Nat. Commun.* **2014**, *5*, 3794. [CrossRef] [PubMed]
6. Franklin, G.L.; Torres-Freyermuth, A. On the Runup Parameterization for Reef-Lined Coasts. *Ocean Model.* **2022**, *169*, 101929. [CrossRef]
7. Gourlay, M.R. Wave Transformation on a Coral Reef. *Coast. Eng.* **1994**, *23*, 17–42. [CrossRef]
8. Pearson, S.G.; Storlazzi, C.D.; van Dongeren, A.R.; Tissier, M.F.S.; Reniers, A.J.H.M. A Bayesian-Based System to Assess Wave-Driven Flooding Hazards on Coral Reef-Lined Coasts. *J. Geophys. Res. Ocean.* **2017**, *122*, 10099–10117. [CrossRef]
9. Quataert, E.; Storlazzi, C.; Rooijen, A.; Cheriton, O.; Dongeren, A. The Influence of Coral Reefs and Climate Change on Wave-Driven Flooding of Tropical Coastlines. *Geophys. Res. Lett.* **2015**, *42*, 6407–6415. [CrossRef]
10. Souter, D.; Planes, S.; Wicquart, J.; Logan, M.; Obura, D.; Staub, F. *Status of Coral Reefs of the World: 2020*; Global Coral Reef Monitoring network (GCRMN) and International Coral Reef Initiative (ICRI): Townsville, Australia, 2021; pp. 1–12.
11. UN-Habitat. *Urbanization and Climate Change in Small Island Developing States*; UN-Habitat: Nairobi, Kenya, 2015.
12. Beck, M.W.; Pfliegner, K.; Quast, O. *Ecosystem-Based Adaptation and Insurance: Success, Challenges and Opportunities*; InsuResilience Secretariat: Bonn, Germany, 2019.
13. Perry, C.T.; Alvarez-Filip, L. Changing Geo-Ecological Functions of Coral Reefs in the Anthropocene. *Funct. Ecol.* **2019**, *33*, 976–988. [CrossRef]
14. Reguero, B.G.; Storlazzi, C.D.; Gibbs, A.E.; Shope, J.B.; Cole, A.D.; Cumming, K.A.; Beck, M.W. The Value of US Coral Reefs for Flood Risk Reduction. *Nat. Sustain.* **2021**, *4*, 688–698. [CrossRef]
15. Sheppard, C.; Dixon, D.J.; Gourlay, M.; Sheppard, A.; Payet, R. Coral Mortality Increases Wave Energy Reaching Shores Protected by Reef Flats: Examples from the Seychelles. *Estuar. Coast. Shelf Sci.* **2005**, *64*, 223–234. [CrossRef]
16. Reguero, B.G.; Secaira, F.; Toimil, A.; Escudero, M.; Díaz-Simal, P.; Beck, M.W.; Silva, R.; Storlazzi, C.; Losada, I.J. The Risk Reduction Benefits of the Mesoamerican Reef in Mexico. *Front. Earth Sci.* **2019**, *7*, 455350. [CrossRef]
17. Harris, D.L.; Vila-concejo, A.; Power, H.E.; Kinsela, M.A.; Webster, J.M. Variability of Depth-Limited Waves in Coral Reef Surf Zones. *Estuar. Coast. Shelf Sci.* **2018**, *211*, 36–44. [CrossRef]
18. Reguero, B.G.; Beck, M.W.; Agostini, V.N.; Kramer, P.; Hancock, B. Coral Reefs for Coastal Protection: A New Methodological Approach and Engineering Case Study in Grenada. *J. Environ. Manag.* **2018**, *210*, 146–161. [CrossRef] [PubMed]
19. Roelvink, F.E.; Storlazzi, C.D.; van Dongeren, A.R.; Pearson, S.G. Coral Reef Restorations Can Be Optimized to Reduce Coastal Flooding Hazards. *Front. Mar. Sci.* **2021**, *8*, 653945. [CrossRef]
20. Storlazzi, C.D.; Reguero, B.G.; Cumming, K.A.; Cole, A.D.; Shope, J.B.; Gaido L, C.; Viehman, T.S.; Nickel, B.A.; Beck, M.W. Rigorously Valuing the Coastal Hazard Risks Reduction Provided by Potential Coral Reef Restoration in Florida and Puerto Rico. In *Open-File Report*; U.S. Geological Survey: Reston, VA, USA, 2021.
21. Fabian, R.; Beck, M.; Potts, D. *Reef Restoration for Coastal Defense*; University of California: Santa Cruz, CA, USA, 2013; pp. 1–59.
22. Morris, R.L.; Konlechner, T.M.; Ghisalberti, M.; Swearer, S.E. From Grey to Green: Efficacy of Eco-Engineering Solutions for Nature-Based Coastal Defence. *Glob. Change Biol.* **2018**, *24*, 1827–1842. [CrossRef]
23. Reguero, B.G.; Beck, M.W.; Bresch, D.N.; Calil, J.; Meliane, I. Comparing the Cost Effectiveness of Nature-Based and Coastal Adaptation: A Case Study from the Gulf Coast of the United States. *PLoS ONE* **2018**, *13*, e0192132. [CrossRef] [PubMed]
24. Silva, R.; Mendoza, E.; Mariño-Tapia, I.; Martínez, M.L.; Escalante, E. An Artificial Reef Improves Coastal Protection and Provides a Base for Coral Recovery. *J. Coast. Res.* **2016**, *1*, 467–471. [CrossRef]

25. Buckley, M.L.; Lowe, R.J.; Hansen, J.E.; Van Dongeren, A.R. Dynamics of Wave Setup over a Steeply Sloping Fringing Reef. *J. Phys. Oceanogr.* **2015**, *45*, 3005–3023. [CrossRef]
26. Van Dongeren, A.; Lowe, R.; Pomeroy, A.; Trang, D.M.; Roelvink, D.; Symonds, G.; Ranasinghe, R. Numerical Modeling of Low-Frequency Wave Dynamics over a Fringing Coral Reef. *Coast. Eng.* **2013**, *73*, 178–190. [CrossRef]
27. Pequignet, A.C.; Becker, J.M.; Merrifield, M.A.; Boc, S.J. The Dissipation of Wind Wave Energy across a Fringing Reef at Ipan, Guam. *Coral Reefs* **2011**, *30*, 71–82. [CrossRef]
28. Nwogu, O.; Demirbilek, Z. Infragravity Wave Motions and Runup over Shallow Fringing Reefs. *J. Waterw. Port Coast. Ocean Eng.* **2010**, *136*, 295–305. [CrossRef]
29. Pomeroy, A.; Lowe, R.; Symonds, G.; Van Dongeren, A.; Moore, C. The Dynamics of Infragravity Wave Transformation over a Fringing Reef. *J. Geophys. Res. Ocean.* **2012**, *117*, C11022. [CrossRef]
30. Symonds, G.; Huntley, D.A.; Bowen, A.J. Two-Dimensional Surf Beat: Long Wave Generation by a Time-Varying Breakpoint. *J. Geophys. Res.* **1982**, *87*, 492–498. [CrossRef]
31. Lowe, R.J.; Falter, J.L.; Bandet, M.D.; Pawlak, G.; Atkinson, M.J.; Monismith, S.G.; Koseff, J.R. Spectral Wave Dissipation over a Barrier Reef. *J. Geophys. Res. C Ocean.* **2005**, *110*, C04001. [CrossRef]
32. Pomeroy, A.W.M.; Lowe, R.J.; Van Dongeren, A.R.; Ghisalberti, M.; Bodde, W.; Roelvink, D. Spectral Wave-Driven Sediment Transport across a Fringing Reef. *Coast. Eng.* **2015**, *98*, 78–94. [CrossRef]
33. Cheriton, O.M.; Storlazzi, C.D.; Rosenberger, K.J. In Situ Observations of Wave Transformation and Infragravity Bore Development Across Reef Flats of Varying Geomorphology. *Front. Mar. Sci.* **2020**, *7*, 351. [CrossRef]
34. Storlazzi, C.D.; Rey, A.E.; Dongeren, A.R.V. A Numerical Study of Geomorphic and Oceanographic Controls on Wave-Driven Runup on Fringing Reefs with Shore-Normal Channels. *J. Mar. Sci. Eng.* **2022**, *10*, 828. [CrossRef]
35. Huang, Z.C.; Lenain, L.; Melville, W.K.; Middleton, J.H.; Reineman, B.; Statom, N.; McCabe, R.M. Dissipation of Wave Energy and Turbulence in a Shallow Coral Reef Lagoon. *J. Geophys. Res. Ocean.* **2012**, *117*, C03015. [CrossRef]
36. Lentz, S.J.; Churchill, J.H.; Davis, K.A.; Farrar, J.T. Surface Gravity Wave Transformation across a Platform Coral Reef in the Red Sea. *J. Geophys. Res. Ocean.* **2016**, *121*, 693–705. [CrossRef]
37. Monismith, S.G.; Rogers, J.S.; Koweek, D.; Dunbar, R.B. Frictional Wave Dissipation on a Remarkably Rough Reef. *Geophys. Res. Lett.* **2015**, *42*, 4063–4071. [CrossRef]
38. Storlazzi, C.D.; Reguero, B.G.; Cole, A.D.; Lowe, E.; Shope, J.B.; Gibbs, A.E.; Nickel, B.A.; McCall, R.T.; van Dongeren, A.R.; Beck, M.W. Rigorously Valuing the Role of U. S. Coral Reefs in Coastal Hazard Risk Reduction. In *Open-File Report 2019–1027*; U.S. Geological Survey: Reston, VA, USA, 2019; Volume 42. [CrossRef]
39. Buckley, M.; Lowe, R.; Hansen, J. Evaluation of Nearshore Wave Models in Steep Reef Environments Topical Collection on the 7th International Conference on Coastal Dynamics in Arcachon, France 24–28 June 2013. *Ocean Dyn.* **2014**, *64*, 847–862. [CrossRef]
40. Lashley, C.H.; Roelvink, D.; van Dongeren, A.; Buckley, M.L.; Lowe, R.J. Nonhydrostatic and Surfbeat Model Predictions of Extreme Wave Run-up in Fringing Reef Environments. *Coast. Eng.* **2018**, *137*, 11–27. [CrossRef]
41. Davis, K.A.; Pawlak, G.; Monismith, S.G. Turbulence and Coral Reefs. *Annu. Rev. Mar. Sci.* **2021**, *13*, 343–373. [CrossRef] [PubMed]
42. Osorio-Cano, J.D.; Alcérreca-Huerta, J.C.; Mariño-Tapia, I.; Osorio, A.F.; Acevedo-Ramírez, C.; Enriquez, C.; Costa, M.; Pereira, P.; Mendoza, E.; Escudero, M.; et al. Effects of Roughness Loss on Reef Hydrodynamics and Coastal Protection: Approaches in Latin America. *Estuaries Coasts* **2019**, *42*, 1742–1760. [CrossRef]
43. Osorio-Cano, J.D.; Alcérreca-Huerta, J.C.; Osorio, A.F.; Oumeraci, H. CFD Modelling of Wave Damping over a Fringing Reef in the Colombian Caribbean. *Coral Reefs* **2018**, *37*, 1093–1108. [CrossRef]
44. Yu, X.; Rosman, J.H.; Hench, J.L. Boundary Layer Dynamics and Bottom Friction in Combined Wave-Current Flows over Large Roughness Elements. *J. Fluid Mech.* **2022**, *931*, A11. [CrossRef]
45. Yu, X.; Rosman, J.H.; Hench, J.L. Interaction of Waves with Idealized High-Relief Bottom Roughness. *J. Geophys. Res. Ocean.* **2018**, *123*, 3038–3059. [CrossRef]
46. Lowe, R.J.; Koseff, J.R.; Monismith, S.G. Oscillatory Flow through Submerged Canopies: 1. Velocity Structure. *J. Geophys. Res. C Ocean.* **2005**, *110*, C10016. [CrossRef]
47. Madsen, O.S. Spectral Wave-Current Bottom Boundary Layer Flows. *Coast. Eng. Proc.* **1994**, *1*, 384–398. [CrossRef]
48. Nielsen, P. *Coastal Bottom Boundary Layers and Sediment Transport*; World Scientific Publishing Company: Singapore, 1992; Volume 4, ISBN 978-981-02-0472-3.
49. Swart, D.H. *Offshore Sediment Transport and Equilibrium Beach Profiles*; TU Delft: Delft, The Netherlands, 1974.
50. Dalrymple, R.A.; Kirby, J.T.; Hwang, P.A. Wave Diffraction Due to Areas of Energy Dissipation. *J. Waterw. Port Coast. Ocean Eng.* **1984**, *110*, 67–79. [CrossRef]
51. Mullarney, J.C.; Henderson, S.M. Flows Within Marine Vegetation Canopies. In *Advances in Coastal Hydraulics*; Panchang, V., Kaihatu, J., Eds.; World Scientific Publishing Ltd.: Singapore, 2018; pp. 1–46.
52. Lowe, R.J.; Falter, J.L.; Koseff, J.R.; Monismith, S.G.; Atkinson, M.J. Spectral Wave Flow Attenuation within Submerged Canopies: Implications for Wave Energy Dissipation. *J. Geophys. Res. Ocean.* **2007**, *112*, C05018. [CrossRef]
53. OpenFOAM. *OpenFOAM User's Guide*; OpenCFD Ltd.: Bracknell, UK, 2020.
54. Le Méhauté, B. *An Introduction to Hydrodynamics and Water Waves*; Springer: Berlin/Heidelberg, Germany, 1967; ISBN 978-3-642-85569-6.

55. Sous, D.; Dodet, G.; Bouchette, F.; Tissier, M. Momentum Balance Across a Barrier Reef. *J. Geophys. Res. Ocean.* **2020**, *125*, e2019JC015503. [CrossRef]
56. Masselink, G.; Tuck, M.; McCall, R.T.; van Dongeren, A.R.; Ford, M.; Kench, P.S. Physical and Numerical Modeling of Infragravity Wave Generation and Transformation on Coral Reef Platforms. *J. Geophys. Res. Ocean.* **2019**, *124*, 1410–1433. [CrossRef]
57. Pomeroy, A.W.M.; Lowe, R.J.; Ghisalberti, M.; Winter, G.; Storlazzi, C.; Cuttler, M. Spatial Variability of Sediment Transport Processes Over Intratidal and Subtidal Timescales Within a Fringing Coral Reef System. *J. Geophys. Res. Earth Surf.* **2018**, *123*, 1013–1034. [CrossRef]
58. Beetham, E.; Kench, P.S.; O'Callaghan, J.; Popinet, S. Wave Transformation and Shoreline Water Level on Funafuti Atoll, Tuvalu. *J. Geophys. Res. Ocean.* **2016**, *121*, 3372–3380. [CrossRef]
59. Boström-Einarsson, L.; Babcock, R.C.; Bayraktarov, E.; Ceccarelli, D.; Cook, N.; Ferse, S.C.A.; Hancock, B.; Harrison, P.; Hein, M.; Shaver, E.; et al. Coral Restoration—A Systematic Review of Current Methods, Successes, Failures and Future Directions. *PLoS ONE* **2020**, *15*, e0226631. [CrossRef]
60. Liu, W.; Liu, Y.; Zhao, X. Numerical Study of Bragg Reflection of Regular Water Waves over Fringing Reefs Based on a Boussinesq Model. *Ocean Eng.* **2019**, *190*, 106415. [CrossRef]
61. Norris, B.K.; Storlazzi, C.D.; Pomeroy, A.W.M.; Rosenberger, K.J.; Logan, J.B.; Cheriton, O.M. Combining Field Observations and High-Resolution Numerical Modeling to Demonstrate the Effect of Coral Reef Roughness on Turbulence and Its Implications for Reef Restoration Design. *Coast. Eng.* **2023**, *184*, 104331. [CrossRef]
62. Larsen, B.E.; Fuhrman, D.R. On the Over-Production of Turbulence beneath Surface Waves in Reynolds-Averaged Navier–Stokes Models. *J. Fluid Mech.* **2018**, *853*, 419–460. [CrossRef]
63. Higuera, P.; Lara, J.L.; Losada, I.J. Realistic Wave Generation and Active Wave Absorption for Navier-Stokes Models. Application to OpenFOAM®. *Coast. Eng.* **2013**, *71*, 102–118. [CrossRef]
64. Buccino, M.; Del Vita, I.; Calabrese, M. Predicting Wave Transmission Past Reef Ball ™ Submerged Breakwaters. *J. Coast. Res.* **2013**, *65*, 171–176. [CrossRef]
65. Henderson, S.M.; Norris, B.K.; Mullarney, J.C.; Bryan, K.R. Wave-Frequency Flows within a near-Bed Vegetation Canopy. *Cont. Shelf Res.* **2017**, *147*, 91–101. [CrossRef]
66. Zeller, R.B.; Zarama, F.J.; Weitzman, J.S.; Koseff, J.R. A Simple and Practical Model for Combined Wave-Current Canopy Flows. *J. Fluid Mech.* **2015**, *767*, 842–880. [CrossRef]
67. Stocking, J.B.; Rippe, J.P.; Reidenbach, M.A. Structure and Dynamics of Turbulent Boundary Layer Flow over Healthy and Algae-Covered Corals. *Coral Reefs* **2016**, *35*, 1047–1059. [CrossRef]
68. Hearn, C.; Atkinson, M.; Falter, J. A Physical Derivation of Nutrient-Uptake Rates in Coral Reefs: Effects of Roughness and Waves. *Coral Reefs* **2001**, *20*, 347–356. [CrossRef]
69. Nakamura, T.; Van Woesik, R. Water-Flow Rates and Passive Diffusion Partially Explain Differential Survival of Corals during the 1998 Bleaching Event. *Mar. Ecol. Prog. Ser.* **2001**, *212*, 301–304. [CrossRef]
70. Ribes, M.; Atkinson, M.J. Effects of Water Velocity on Picoplankton Uptake by Coral Reef Communities. *Coral Reefs* **2007**, *26*, 413–421. [CrossRef]
71. Reidenbach, M.A.; Stocking, J.B.; Szczyrba, L.; Wendelken, C. Hydrodynamic Interactions with Coral Topography and Its Impact on Larval Settlement. *Coral Reefs* **2021**, *40*, 505–519. [CrossRef]